Numerical simulation of Joule heating and Arrhenius activation energy for nonlinear radiative flow of Casson nanofluid with Cattaneo–Christov heat flux model

M Ijaz[1,4] , **M S Alqarni**[2], **F Salah**[3] and **M Y Malik**[2]

[1] Department of Mathematics, Quaid-I-Azam University 45320, Islamabad 44000, Pakistan
[2] Department of Mathematics, College of Science, King Khalid University, Abha 61413, Kingdom of Saudi Arabia
[3] Department of Mathematics, Faculty of Science and Arts, King Abdul-Aziz University, Jeddah, Kingdom of Saudi Arabia

E-mail: misbahijaz@math.qau.edu.pk

CrossMark

Abstract

This article explores the novel features of Cattaneo–Christov heat flux model for nonlinear radiative flow of Casson nanofluid over an inclined permeable stretched cylinder with joule heating mechanism. The novelty of the present study is to account for the effect of activation energy, dual stratification, nonlinear mixed convection, non-uniform heat generation/absorption, binary chemical reaction and Joule heating effect. The velocity and thermal slips are also accounted for present flow model instead of no-slip condition. Casson fluid nanomaterial model is measured that refers to the significant slip mechanism such as Brownian and thermophoresis diffusions. Suitable similarity transformations are employed to get the required coupled ODEs system. The developed nonlinear system is unravelled through shooting technique along with Runge–Kutta–Fehlberg (RK-45) approach. Physical quantities of interest are investigated through graphs and tables. From the present analysis, we will see the conflicting effect of chemical reaction parameter (γ_3) to that of activation energy parameter (E_a). Further it will be also analyzed that the heat transfer rate at the cylindrical surface and thermal boundary layer thickness enhances within the frame thermal radiation (N_r). It will also be observed that both thermophoresis (N_t) and activation energy parameter become a source of enhancement in concentration frame. A validation of the work is offered by comparing the current results with published literature. Casson flow model as deliberated in the paper finds practical applications in polymer engineering, blood flow, silicon suspensions, and lithograph industry.

Keywords: Casson fluid model, Arrhenius activation energy, Joule heating, nonlinear thermal radiation, Cattaneo–Christov heat flux model, shooting method, non-uniform heat generation/absorption

(Some figures may appear in colour only in the online journal)

Nomenclature

B_o	magnetic field strength (A m^{-1})
(B_1, B_2)	space and temperature dependent heat source/sink coefficient
(C_o, C_w, C_∞)	reference, surface and ambient concentration
D_B	Brownian diffusion coefficient (m^2 s^{-1})

[4] Author to whom any correspondence should be addressed.

D_T	thermophoretic diffusion coefficient ($m^2\,s^{-1}$)
E_l	activation energy ($KJ\,mol^{-1}$)
Ec	Eckert number
E_a	activation energy parameter
$G(\eta)$	similarity function
$\hat{g}_l$	gravitational acceleration ($m\,s^{-2}$)
$\hat{k}_f$	fluid thermal conductivity ($W\,mK^{-1}$)
$\hat{K}_r^2$	chemical reaction rate constant
k^*	Boltzmann constant ($eV\,K^{-1}$)
M_l	Hartman number
$\hat{N}_l$	Buoyancy ratio forces
N_b	Brownian motion parameter
N_t	thermophors parameter
N_r	radiation parameter
Pr	Prandtl number
p	fitted rate constant
$\mathbf{q}_l$	heat flux ($W\,m^{-2}$)
(S_v, S_t)	velocity and thermal slip parameters
(S_1, S_2)	thermal and solutal stratification parameters
Sc	Schmidt number
(T_o, T_w, T_∞)	reference, surface and ambient temperature (K)
V_2	velocity slip factor
V_p	mass transfer parameter
(w_1, u_1)	velocity components ($m\,s^{-1}$)

Greek symbols

ρ_f	fluid density ($kg\,m^{-3}$)
ν_1	kinematic viscosity ($m^2\,s^{-1}$)
γ_1	curvature parameter
γ_2	chemical reaction parameter
γ_3	reaction rate constant
ϕ_1	angle of inclination (Rad)
Φ_1	dimensionless nanoparticle concentration
β_1	mixed convection parameter
(β_t, β_c)	nonlinear thermal and solutal convection parameters
Θ_1	dimensionless temperature
Θ_w	temperature ratio parameter
τ_w	surface shear stress ($N\,m^{-2}$)
δ	temperature difference (K)
$(\rho c_p)_f$	heat capacity of basefluid ($J\,K^{-1}$)
$(\rho c_p)_p$	effective heat capacity of nanoparticle material ($J\,K^{-1}$)
σ_3	electrical conductivity of base fluid ($S\,m^{-1}$)

(Γ_1, Γ_3)	linear thermal expansion coefficients
(Γ_2, Γ_4)	nonlinear solutal expansion coefficients
$\hat{\Gamma}_e$	thermal relaxation time

Introduction

The role of radiative heat transfer is quite phenomenal in various engineering processes like nuclear power plants, process of solar heat generation hypersonic flights, gas turbines, space vehicles, gas cooled nuclear reactors etc. Radiation does not involve any medium for prorogation but depends on the features like solid geometric arrangement, temperature and surface properties of the that are emitting or absorbing heat. It is substantial to notice that the linear is not effectively valid for excessive temperature difference because the dimensionless parameter that is used in the linearized Rosseland approximation is only the effective Prandtl number [1], whereas in the nonlinear approximation, the problem is directed through three parameters, such as Prandtl number, the radiation parameter and the temperature ratio parameter. Heat exchange influenced by thermal radiation has marvellous applications in numerous technological procedures including satellites, missiles and space vehicles. Pantokratoras [2] studied the influence of nonlinear and linear Rosseland radiation on steady laminar natural convection along a normal isothermal plate by means of a novel radiation parameter named as film radiation parameter. Cortell [3] accomplish a numerical procedure in association with the boundary layer flow induced in a quiescent fluid by a constant stretching sheet in the presence of nonlinear Rosseland thermal radiation. Parida *et al* [4] considered two-dimensional MHD boundary layer flow of heat and mass transfer over a horizontal plate with partial slip at the surface subjected to the convective heat flux in the view of nonlinear thermal radiation Bhatti *et al* [5] explored heat transfer with nonlinear thermal radiation on sinusoidal motion of magnetic dense particles in a dusty fluid. Recent development can be seen via [6–9].

The study of complex mechanism of non-Newtonian fluid exhibits great challenge for Physicists, Engineers and Mathematicians. The conventional Navier–Stokes equation does not predict all features of such complex fluids. Therefore, developments of numerous rheological models are the obligation of the time [10–18]. The applications of nonlinear fluids are common in geophysics, petroleum procedures and chemical industry. Condensed milk, toothpaste, mud, fruit puree, foams, certain oils, ketchup, soaps and lubricants are some examples of non-Newtonian fluids. The viscoplasticity of non-Newtonian fluid is characterized by a yield stress, below which the fluid has infinite viscosity (at zero shear rate) and above which it has zero viscosity (at infinite shear rate). Thus, Casson fluid behaves like solid as well as viscoplastic fluid depending on shear rate of fluid. The most significant viscoplastic models are Bingham model [19], Herschel–Bulkley model [20] and the Casson fluid model [21, 22]. All these ideal rheological models are discontinuous. The most popular among these models is the Casson fluid model. Casson fluid can be defined as a shear thinning liquid which is

supposed to have an infinite viscosity at zero rate of shear, a yield stress below which no flow arises and a zero viscosity at an infinite rate of shear [23–25]. This model has been utilized for relating the steady shear stress-shear irate behavior of blood, tomato puree, yogurt, molten chocolate, honey, jelly, etc. Human blood can also be figure out as Cassonifluid when flowing through small arteries. Eldabe and Salwa [26] have investigated the flow of Casson fluid between two rotating cylinders. Boyd *et al* [27] inspected the steady and oscillatory flows of the Casson and Carreau–Yasuda non-Newtonian blood models via lattice Boltzmann method. Nadeem *et al* [28] investigated three-dimensional flow of Casson fluid over a linearly stretched sheet in the presence of an external magnetic field. Dash *et al* [29] analyzed the characteristic of Casson fluid under yield stress in a circular tube of homogeneous porous medium.

Stratification [30] is a phenomenon that arises in flow field due to variation in temperature, concentration and densities of the fluid. Wave phenomena in airflow over mountains and occurrence of smog are particular examples of stratification in the atmosphere. In stratification phenomena, significant density variation of fluid occurs in a vertical direction. Some applications of stratification are heat rejection from environment like lake, thermal storage system like solar ponds, hermo-hydraulic, geothermal systems, transference of heat from thermal sources like power plant condenser and many others. In natural reservoir, the growth rate of unicellular/multicellular organism is directly affected by controlling the temperature and concentration differences of hydrogen and oxygen by means of stratification. Hayat *et al* [31] measured the impact of thermal stratification on mixed convective Maxwell fluid flow. Ijaz *et al* [32] discussed the dual stratification phenomena for nonlinear convective flow of Maxwell nanofluid in presence of binary chemical reaction and activation energy. Influences of thermal radiation and thermal stratification of thixotropic fluid are scrutinized by Shehzad *et al* [33]. Ibrahim and Makinde [34] explored the mixed convection flow of nanofluid with dual stratification. Ijaz *et al* [35] studied the stratified flow of ferromagnetic Maxwell nanofluid in view of viscous dissipation and heat generation/absorption. Some additional research regarding stratified flows of non-Newtonian models can be viewed via [36–38].

Heat transfer phenomena have been debated through conventional Fourier's law [39] of heat conduction from many decades. Fourier's law of heat provides us a parabolic form of energy expression which shows that the entire framework is instantly influenced by the primary disturbance. Cattaneo [40] modified this matter by introducing thermal relaxation time in the Fourier's expression that yields hyperbolic form of energy equation. Christov [41] improved the study of Cattaneo by presenting thermal relaxation time in terms of Oldroyd's upper-convected derivatives for material-invariant formulation. This modification is well-known as Cattaneo–Christov heat flux model. The thermal instability in porous medium is discussed by Hadded [42] through Cattaneo–Christov heat flux model.

The aim of present study is to discover the novel characteristics of activation energy in nonlinearly radiative flow of Casson nanomaterial with velocity and thermal slip conditions over an inclined permeable stretched cylinder. Modified
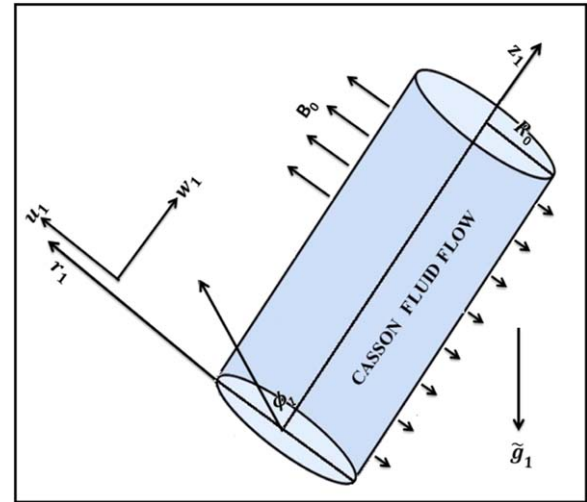

Figure 1. Flow geometry.

Arrhenius formula for activation energy is employed with binary chemical reaction. Generalized Fourier's law of heat conduction is also utilized through Cattaneo–Christov heat flux model. The novelty of problem is to explore the features of activation energy for Casson model in view of Joule heating, non-uniform heat generation/absorption, double stratification and nonlinear mixed convection with slip mechanism. Nonlinear differential equations are elucidated numerically by Shooting method in assistance of Runge–Kutta Fehlberg method [43, 44]. Graphs and tables are designed to study the behavior of eminent variables on fluid characteristics.

Modeling strategy

Here we consider two-dimensional, nonlinear radiative flow of Cassoni nanofluid over an inclined stretched cylinder of radius (R_o). The coordinates r_1 and z_1 are selected along radial and axial directions of cylinder. Fluid flow is maintained due to linear stretching velocity of the form $W_w \left(= \frac{W_o z_1}{L} \right)$. Present analysis has been accomplished with Joule heating, nonlinear thermal radiation, non-uniform heat source/sink, thermal and solutal stratification, nonlinear mixed convection, binary chemical reaction and Arrhenius activation energy. The velocity and thermal slip are also inspected for present flow problem. The uniform magnetic field of effective strength (B_o) is applied in the radial direction of the cylinder (see figure 1). Here, heat transfer phenomenon is analyzed with the Cattaneo–Christov heat flux theory. Temperature and concentration at the surface of cylinder are maintained at (T_w) and (C_w) while ambient fluid temperature and concentration are kept at (T_∞) and (C_∞), respectively. The rheological expression of Casson fluid can be expressed as follows [21–23]:

$$\hat{\tau}_{ij} = \begin{cases} 2\left(\mu_p + \dfrac{\hat{\tau}_o}{\sqrt{2\pi_c}}\right)\bar{e}_{ij}, \ \pi > \pi_c \\ 2\left(\mu_p + \dfrac{\hat{\tau}_o}{\sqrt{2\pi_c}}\right)\bar{e}_{ij}, \ \pi < \pi_c \end{cases}, \qquad (1)$$

In the above equation, $\pi = \overline{e}_{ij}.\overline{e}_{ij}$ is defined as product of component of deformation rate with itself. While (π_c), (π_p) and $(\hat{\tau}_o)$ are the critical value of Casson fluid, plastic dynamic viscosity and yield stress of non-Newtonian fluid. Casson fluid model is reduced to a viscous fluid at very high wall shear stresses provided that wall stress is much greater than yield stress. This fluid shows good approximations for many substances which include molten chocolate, biological materials, nail polish, cosmetics, some particulate suspensions etc.

conductivity and $\hat{\Gamma}_e$ for thermal relaxation time, respectively. Fundamental Fourier's law is deduced by putting $\hat{\Gamma}_e = 0$ in equation (5). Due to existence of thermal relaxation time factor ($\xi_3 \neq 0$), the paradox of heat conduction is rectified.

For incompressible and steady flow assumptions [46]

$$\mathbf{q}_1 + \hat{\Gamma}_e[\mathbf{V}_c.\nabla\mathbf{q}_1 - \mathbf{q}_1.\nabla\mathbf{V}_c] = -\hat{k}_f\nabla T. \quad (5)$$

Energy and concentration expressions within the frame of assumptions are [47]

$$
\left.
\begin{aligned}
u_1\frac{\partial T}{\partial r_1} + w_1\frac{\partial T}{\partial z_1} + \hat{\Gamma}_e\hat{\Omega}_e &= \frac{\hat{k}_f}{(\rho C_p)_f}\frac{1}{r_1}\frac{\partial}{\partial r_1}\left(r_1\frac{\partial T}{\partial r_1}\right) + \frac{\mu}{(\rho C_p)_f}\left(1 + \frac{1}{\xi_1}\right)\left(\frac{\partial w_1}{\partial r_1}\right)^2 \\
&+ \frac{1}{(\rho C_p)_f}\frac{1}{r_1}\frac{\partial}{\partial r_1}\left(\frac{16\hat{\sigma}_3 T^3}{3\hat{K}_2}r_1\frac{\partial T}{\partial r_1}\right) + \frac{\sigma_3 B_o^2 w_1^2}{\rho_f} + \frac{\hat{Q}_m}{(\rho C_p)_f} \\
&+ \tau_1 D_B\left(\frac{\partial C}{\partial r_1}\frac{\partial T}{\partial r_1}\right) + \frac{\tau_1 D_T}{T_\infty}\left(\frac{\partial T}{\partial r_1}\right)^2
\end{aligned}
\right\} \quad (6)
$$

For steady two-dimensional flow governing expressions in the absence of pressure gradient along with boundary layer approximations are [24–41]:

$$\frac{\partial}{\partial r_1}(r_1 u_1) + \frac{\partial}{\partial z_1}(r_1 w_1) = 0, \quad (2)$$

$$
\left.
\begin{aligned}
w_1\frac{\partial w_1}{\partial z_1} + u_1\frac{\partial w_1}{\partial r_1} &= \frac{\nu_1}{r_1}\left(1 + \frac{1}{\xi_1}\right)\frac{\partial}{\partial r_1}\left(r_1\frac{\partial w_1}{\partial r_1}\right) \\
&- \frac{\sigma_3 B_o^2 w_1}{\rho_f} + \frac{\hat{g}_1}{\rho_f}[\Gamma_1(T - T_\infty) + \Gamma_2(T - T_\infty)^2 \\
&+ \Gamma_3(C - C_\infty) + \Gamma_4(C - C_\infty)^2]\cos\phi_1,
\end{aligned}
\right\} \quad (3)
$$

For modeling of equation (2), law of conservation of mass has been used which states that total mass of the system remains constant over time. Here momentum equation is derived based on Newton's second law under the influence of MHD and gravitational force. Flow analysis has been accomplished by neglecting the external electric field, the induced magnetic field and the electric field due to polarization of charges.

Energy equation via Fourier's law is of parabolic type which shows that the whole system is immediately affected by the primary disturbance. This issue has been controlled through the thermal relaxation time in the Fourier's law (see Cattaneo [39]). In 2009, Christov (see [41]) improved the analysis of Cattaneo [40] by introducing thermal relaxation time and using Oldroyd's upper convected derivatives for the material-invariant formulation.

Cattaneo–Christove heat flux model [45] is

$$\mathbf{q}_1 + \hat{\Gamma}_e\left[\frac{\partial\mathbf{q}_1}{\partial t} + \mathbf{V}_c.\nabla\mathbf{q}_1 - \mathbf{q}_1.\nabla\mathbf{V}_c + (\nabla.\mathbf{V}_c)\mathbf{q}_1\right] = -\hat{k}_f\nabla T,$$

$$(4)$$

where $\mathbf{q}_1$ defines for heat flux, $\hat{k}_f$ for fluid thermal

$$
u_1\frac{\partial C}{\partial r_1} + w_1\frac{\partial C}{\partial z_1} = \frac{D_B}{r_1}\frac{\partial}{\partial r_1}\left(r_1\frac{\partial C}{\partial r_1}\right)
$$
$$
+ \frac{D_T}{T_\infty}\frac{1}{r_1}\frac{\partial}{\partial r_1}\left(r_1\frac{\partial T}{\partial r_1}\right) - \hat{K}_a - \hat{K}_1(C - C_\infty). \quad (7)
$$

The corresponding boundary conditions are [48]

$$
\left.
\begin{aligned}
w_1 &= \frac{W_o z_1}{L_1} + V_2\left(1 + \frac{1}{\xi_1}\right)\frac{\partial w_1}{\partial r_1}, \quad u_1 = V_1 \\
T &= T_o + \frac{d_1 z_1}{L_1} + V_3\frac{\partial w_1}{\partial r_1}, \qquad C = C_o + \frac{d_3 z_1}{L_1}
\end{aligned}
\right|
$$
at $r_1 = R_o,$ $\quad(8)$

$$
\left.
\begin{aligned}
w_1 &\to 0, \quad T \to T_\infty = T_o + \frac{d_2 z_1}{L_1} \\
u_1 &\to 0, \quad C \to C_\infty = C_o + \frac{d_4 z_1}{L_1}
\end{aligned}
\right|
\text{as } r_1 \to \infty, \quad (9)
$$

With

$$
\left.
\begin{aligned}
\hat{\Omega}_e &= u_1^2\frac{\partial^2 T}{\partial r_1^2} + w_1^2\frac{\partial^2 T}{\partial z_1^2} + \frac{\partial T}{\partial r_1}\left(w_1\frac{\partial u_1}{\partial z_1} + u_1\frac{\partial u_1}{\partial r_1}\right) \\
&+ 2w_1 u_1\frac{\partial^2 w_1}{\partial r_1\partial z_1} + \left(w_1\frac{\partial w_1}{\partial z_1} + u_1\frac{\partial w_1}{\partial r_1}\right)\frac{\partial T}{\partial z_1},
\end{aligned}
\right\} \quad (10)
$$

here (u_1, w_1) symbolizes for the velocity components in r_1 and z_1-directions respectively, ξ_1 for material parameter, ρ_f for fluid density, (Φ_1) for angle of inclination, $\nu_1\left(\left(=\frac{\mu}{\rho}\right)_f\right)$ for kinematic viscosity, $(\hat{g}_1)$ for gravitational acceleration, (L_1) for

characteristic length of the cylinder, (T_o, C_o) for temperature and concentration, (Γ_1, Γ_2) for linear and nonlinear thermal expansion coefficients, (Γ_3, Γ_4) for linear and nonlinear solutal expansion coefficients, (V_2) for velocity slip factor, $(\hat{K}_1)$ for chemical reaction parameter, (σ_3) for electrical conductivity, $(C_p)_f$ for specific heat, $(\hat{K}_2)$ for mean absorption coefficient, $(\hat{\sigma}_3)$ for Stefan–Boltzmann constant and (D_B, D_T) for Brownian and themophoretic diffusion coefficients, respectively.

The mathematical expression of non-uniform heat generation/absorption is [49]:

$$\hat{Q}_m = \frac{W_w(z_1)\hat{k}_f}{z_1 \nu_1}\left[B_1(T_w - T_o)\frac{\partial G}{\partial \eta} + B_2 (T - T_\infty)\right], \quad (11)$$

here $B_1(>0)$ and $B_2 (>0)$ represent heat generation state of system while $B_1(<0)$ and $B_2 (<0)$ resembles for heat absorption.

Arrhenius equation gives the dependence of the rate constant of a chemical reaction on the absolute temperature, a pre-exponential factor and other constants of the reaction. The Arrhenius law is normally of the following form [50]:

$$\hat{K}_a = \hat{K}_r^2\left(\frac{T}{T_\infty}\right)^p \exp\left[-\frac{E_1}{Tk*}\right], \quad (12)$$

where $\hat{K}_a$ is the rate constant of chemical reaction and $\hat{K}_r^2$ is the preexponential factor based on the fact that enhancing the temperature frequently causes a noticeable increase in the rate of reactions. E_1 is the activation energy and $k* = 8.61 \times 10^{-5}$ eV K^{-1} is the Boltzmann constant which is the physical constant relating energy at the individual particle level with temperature observed at the bulk level. This equation has vast applications in determining rate of chemical reactions and for calculation of energy of activation.

Apposite transformations for present flow are [51]:

$$\left.\begin{array}{l} \eta = \sqrt{\frac{W_o}{\nu_1 L_1}}\left(\frac{r_1^2 - R_o^2}{2R_o}\right), \qquad w_1(\eta) = \frac{W_o z_1}{L_1}G'(\eta), \quad \Psi(\eta) = \sqrt{\frac{\nu_1 W_o z_1 R_o^2}{L_1}}\,G(\eta), \\[3mm] u_1(\eta) = -\frac{R_o}{r_1}\sqrt{\frac{\nu_1 W_o}{L_1}}\,G(\eta), \quad \Theta_1(\eta) = \frac{T - T_\infty}{T_w - T_o}, \qquad \phi_1(\eta) = \frac{C - C_\infty}{C_w - C_o}, \end{array}\right\} \quad (13)$$

The transformed flow expressions are [52]:

$$\left.\begin{array}{l} (1 + 2\gamma_1\eta)\left(1 + \frac{1}{\xi_1}\right)G''' + 2\gamma_1\left(1 + \frac{1}{\xi_1}\right)G'' + GG'' - G'^2 \\[3mm] + \beta_1[(1 + \beta_t\Theta_1)\Theta_1 + \hat{N}_1(1 + \beta_c\phi_1)\phi_1]\cos\Phi_1 - M_1 G' = 0, \end{array}\right\} \quad (14)$$

$$\left.\begin{array}{l} (1 + 2\gamma_1\eta)\left(\Theta_1'' + PrN_b\left(\Theta_1'\phi_1' + \frac{N_t}{N_b}\Theta_1'^2 + Ec\left(1 + \frac{1}{\xi_1}\right)G''^2\right)\right) + 2\gamma_1\Theta_1' \\[3mm] + PrG\Theta_1' + [1 + N_r(1 + (\Theta_w - 1)\Theta_1)^3\Theta_1']' + (B_1 G' + B_2\Theta_1) + M_1 G'^2 \\[3mm] + Pr\delta_e[(S_1 + \Theta_1)(GG'' - G'^2) + GG'\Theta_1' - \Theta_1''G^2] - Pr(S_1 + \Theta_1)G' = 0, \end{array}\right\} \quad (15)$$

$$\left.\begin{array}{l} (1 + 2\gamma_1\eta)\left(\phi_1'' + \frac{N_t}{N_b}\Theta_1''\right) + 2\gamma_1\phi_1' + 2\gamma_1\left(\frac{N_t}{N_b}\right)\Theta_1' + ScG\phi_1' \\[3mm] - Sc(S_2 + \phi_1)G' + \gamma_2\phi_1 - Sc\gamma_3(1 + \delta\Theta_1)^p \exp\left[-\frac{E_a}{(1 + \delta\Theta_1)}\right] = 0, \end{array}\right\} \quad (16)$$

$$\left.\begin{array}{ll} G'(0)i = 1 + S_v\left(1 + \frac{1}{\xi_1}\right)G''(0), \quad G(0) = V_p, \qquad \Theta_1(0)i = 1 - S_1 + S_t\Theta_1'(0), \\[3mm] \phi_1(0)i = 1 - S_2, \qquad\qquad\qquad G'(\infty) \to i0, \quad \Theta_1(\infty) \to i0, \\[3mm] \phi_1(\infty) \to i0. \end{array}\right\} \quad (17)$$

Here, (γ_1) symbolizes for curvature parameter, (β_1) for mixed convection parameter, (Sc) for Schmidt number, (β_t, β_c) nonlinear thermal and solutal convection parameters, (N_r) for radiation parameter, (Θ_w) for temperature ratio parameter, (Pr) for Prandtl number, (M_1) for Hartman number, ($\hat{N}_1$) for ratio of concentration to thermal bouncy forces, (N_b, N_t) for Brownian motion and thermophorsis parameters, (S_1, S_2) for thermal and solutal stratification parameters, (γ_2) for chemical reaction, (δ) for temperature difference, (Ec) for Eckert number, (E_a) for activation energy, (γ_3) for reaction rate constant, (S_v, S_t) for velocity and thermal slip parameters, respectively.

Emerging flow parameters are defined as [53]

$$
\left.
\begin{aligned}
&\gamma_1 = \sqrt{\frac{\nu_1 L_1}{R_o^2 W_o}}, && Gr = \frac{\Gamma_1 \hat{g}_1 (T_w - T_o) z_1^3}{\nu_1^2}, && \delta = \frac{T_w - T_o}{T_\infty}, \\
&S_v = \frac{V_2 r_1}{R_o} \sqrt{\frac{W_o}{\nu_1 L_1}}, && Gr^* = \frac{\Gamma_3 \hat{g}_1 (C_w - C_o) z_1^3}{\nu_1^2} && Pr = \frac{\nu_1 C_p}{\hat{k}_f}, \\
&\beta_c = \frac{\Gamma_4 (C_w - C_o)}{\Gamma_3}, && N_t = \frac{\tau_1 D_T (T_w - T_o)}{T_\infty \nu_1} && \gamma_2 = \frac{\hat{K}_1 L_1}{W_o}, \\
&\beta_t = \frac{\Gamma_2 (T_w - T_o)}{\Gamma_1}, && N_b = \frac{\tau_1 D_B (C_w - C_o)}{\nu_1} && \gamma_3 = \frac{K_r^2 L_1}{W_o}, \\
&M_1 = \sqrt{\frac{\sigma_2 B_o^2 L_1}{W_o \rho}}, && \hat{N}_1 = \frac{\Gamma_3 (C_w - C_o)}{\Gamma_1 (T_w - T_o)}, && E_a = \frac{E_1}{T_\infty k^*}, \\
&Ec = \frac{W_w^2}{C_p (T_w - T_o)}, && \beta_1 = \frac{Gr}{Re_{z_1}^2}, && \delta_e = \frac{U_o \Gamma_e}{L_1}, \\
&S_1 = \frac{d_2}{d_1}, \ Sc = \frac{\nu_1}{D_B}, && S_2 = \frac{d_4}{d_3}.
\end{aligned}
\right\}
$$

$$(18)$$

The engineering design quantities include skin-friction coefficient, the local Nusselt number and the local Sherwood number. Mathematically, skin friction coefficient C_G, local Nusselt Nu_{z_1} and Sherwood Sh_{z_1} numbers are [54]:

$$
C_G = \frac{2\tau_w}{\rho W_w^2}, \ Nu_{z_1} = \frac{z_1 q_w}{\hat{k}_f (T_w - T_o)}, \ Sh_{z_1} = \frac{z_1 q_m}{D_B (C_w - C_o)},
$$
$$(19)$$

with

$$
\left.
\begin{aligned}
\tau_w &= \left| \mu \left(1 + \frac{1}{\xi_1}\right) \frac{\partial w_1}{\partial r_1} \right|_{r_1 = R_o}, \\
q_w &= -\left| \hat{k}_f \frac{\partial T}{\partial r_1} \right|_{r_1 = R_o} + (q_r)_w \\
q_m &= -\left| D_B \frac{\partial C}{\partial r_1} \right|_{r_1 = R_o}.
\end{aligned}
\right\}
$$
$$(20)$$

In which $(q_r)_w$ is defined as

$$
(q_r)_w = -\frac{16 \hat{\sigma}_3 T^3}{3 \hat{K}_2} \frac{\partial T}{\partial r_1} \bigg|_{r_1 = R_o},
$$
$$(21)$$

The dimensionless forms of (C_G), (Nu_{z_1}) and (Sh_{z_1}) are

$$
\left.
\begin{aligned}
&\frac{1}{2} C_G (Re_{z_1})^{\frac{1}{2}} = \left(1 + \frac{1}{\xi_1}\right) G''(0), \\
&Nu_{z_1} (Re_{z_1})^{-\frac{1}{2}} = -(1 + N_r(1 + (\Theta_w - 1)\Theta_1(0))^3)\Theta_1'(0), \\
&Sh_{z_1} (Re_{z_1})^{-\frac{1}{2}} = -\phi_1'(0),
\end{aligned}
\right\}
$$
$$(22)$$

where, $Re_{z_1}\left(= \frac{W_o z_1^2}{L_1}\right)$ is the local Reynold number.

Computational algorithm and validation

The numerical solution of resulting system of coupled nonlinear ODEs (equations (14)–(16)) along with boundary conditions equation (17) is computed by means of shooting technique along with fifth order Runge–Kutta Felberg method [55] in MATLAB software with $\xi = 0.001$. Newton method is applied for the modification of initial guesses U_1, U_2 and U_3 subjected to the tolerance of $\varepsilon = 10^{-7}$. For present study, the domain of the problem is considered as $[0 - 15]$ instead of $[0 - \infty)$. To proceed with such technique, we have to reduce higher order coupled system into the first order equivalent system by defining new variables $(Z_1, Z_2, Z_3, Z_4, Z_5, Z_6, Z_7) = (G, G', G'', \Theta_1, \Theta_1', \phi_1, \phi_1')$. The first order equivalent system in term of Z_i for $(i = 1, 2, 3, 4, 5, 6, 7)$ is

$$
Z_1' = Z_2,
$$
$$(23)$$

$$
Z_2' = Z_3,
$$
$$(24)$$

$$
Z_3' = \frac{\left(
\begin{aligned}
&-2\gamma_1\left(1 + \frac{1}{\xi_1}\right)Z_3 - Z_1 Z_3 + Z_2^2 + M_1^2 Z_2 - \\
&\beta_1((1 + \beta_t Z_4)Z_4 + \hat{N}_1(1 + \beta_c Z_6)Z_6)\cos \Phi_1
\end{aligned}
\right)}{(1 + 2\gamma_1 \eta)\left(1 + \frac{1}{\xi_1}\right)},
$$
$$(25)$$

$$
Z_4' = Z_5,
$$
$$(26)$$

Table 1. Comparison of $\left(1+\frac{1}{\xi_1}\right)G''(0)$ with [57].

		$-\left(1+\frac{1}{\xi_1}\right)G''(0)$	
ξ_1	M_1	[58]	Present
∞	0	1.0042	1.000 02
5		−1.0954	−1.095 44
1		−1.4142	−1.414 25
∞	10	−3.3165	−3.316 63
5		−3.6331	−3.633 17
1		−4.6904	−4.690 44
∞	100	−10.049	−10.049 86
5		−11.0091	−11.009 07
1		−14.2127	−14.212 65

Table 2. Comparison of $Nu_{z_1}(Re_{z_1})^{-\frac{1}{2}}$ with [58] and [59].

Pr.	[58] $\begin{pmatrix}St = S \\ = M_1\end{pmatrix}$	[59] $\begin{pmatrix}E_a = \gamma_1 \\ = 0\end{pmatrix}$	Present $\begin{pmatrix}\xi_1 \to \infty,\ \gamma_1 = S_1 = M_1 = \\ \beta_1 = B_1 = B_2 = N_r = 0\end{pmatrix}$
1.0	0.9547	0.9547	0.9546
2.0	1.4714	1.4714	1.4714
3.0	1.8961	1.8961	1.8960

Table 3. Numerical values of $\frac{1}{2}C_G(Re_{z_1})^{\frac{1}{2}}$ towards various physical parameters.

γ_1	ξ_1	β_1	M_1	S_1	E_a	S_2	$-\left(1+\frac{1}{\xi_1}\right)G''(0)$ Shooting	Bvp4c
0.2							2.2045	2.2045
0.4							3.0085	3.0085
0.6							4.0523	4.0523
	1.1						1.7581	1.7581
	1.3						1.7845	1.7845
	1.5						1.8073	1.8073
		0.2					1.6547	1.6547
		0.4					1.5278	1.5278
		0.6					1.3785	1.3785
			0.1				1.5674	1.5674
			0.3				1.7967	1.7967
			0.5				1.9653	1.9653
				0.2			1.7455	1.7455
				0.4			1.7697	1.7697
				0.6			1.7863	1.7863
					0.4		1.9788	1.9788
					0.8		1.4875	1.4875
					1.2		1.0753	1.0753
						0.1	1.7486	1.7486
						0.3	1.7355	1.7355
						0.5	1.7243	1.7243

$$Z_5' = \frac{\begin{pmatrix} -(1 + 2\gamma_1\eta)Pr\left(N_b Z_5 Z_7 + N_t Z_5^2 + Ec\left(1 + \frac{1}{\xi_1}\right)Z_3^2\right) - Pr Z_1 Z_5 \\ + Pr(S_1 + Z_4)Z_2 - 2\gamma_1 Z_5 - [1 + N_r(1 + (\Theta_w - 1)Z_4)^3 Z_5]' \\ - Pr\delta_e((S_1 + Z_4)(Z_1 Z_3 - Z_2^2) + Z_1 Z_2 Z_5) - (B_1 Z_2 + B_2 Z_4) \end{pmatrix}}{(1 + 2\gamma_1\eta - Pr\delta_e Z_1^2)}, \tag{27}$$

$$Z_6' = Z_7, \tag{28}$$

$$Z_7' = \frac{\begin{pmatrix} -\dfrac{N_t}{N_b}((1 + 2\gamma_1\eta)Z_5' + 2\gamma_1 Z_5) - \gamma_2 Z_6 - Sc Z_1 Z_7 - 2\gamma_1 Z_7 \\ + Sc(S_2 + Z_6)Z_2 + Sc\gamma_3(1 + \delta Z_4)^p \exp\left[-\dfrac{E_a}{(1 + \delta Z_4)}\right] \end{pmatrix}}{(1 + 2\gamma_1\eta)}, \tag{29}$$

With

$$\left.\begin{array}{l} Z_1(0) = V_p, \qquad Z_2(0) = S_v\left(1 + \dfrac{1}{\xi_1}\right)U_1, \ Z_3(0) = U_1 \\ Z_4(0) = 1 - S_1, \ Z_5(0) = U_2 \qquad\qquad Z_6(0) = 1 - S_2, \\ Z_7(0) = U_3, \end{array}\right\} \tag{30}$$

Table 4. Numerical values of $Nu_{z_1}(Re_{z_1})^{-\frac{1}{2}}$ towards various physical parameters.

γ_1	ξ_l	N_r	δ_e	S_1	E_a	B_1	$-Nu_{z_1}(Re_{z_1})^{-\frac{1}{2}}$	
							Shooting	Bvp4c
0.2							0.6254	0.6254
0.4							0.7367	0.7367
0.6							0.8498	0.8498
	1.1						0.7568	0.7568
	1.3						0.7365	0.7365
	1.5						0.7149	0.7149
		1.0					0.7857	0.7857
		2.0					0.7286	0.7286
		3.0					0.6394	0.6394
			0.3				0.7465	0.7465
			0.5				0.7389	0.7389
			0.7				0.7266	0.7266
				0.2			0.7465	0.7465
				0.4			0.7387	0.7387
				0.6			0.7259	0.7259
					0.0		0.8854	0.8854
					1.0		1.0657	1.0657
					2.0		1.8784	1.8784
						0.1	0.7593	0.7593
						0.3	0.7048	0.7048
						0.5	0.6532	0.6532

Table 5. Numerical values of $Sh_{z_1}(Re_{z_1})^{-\frac{1}{2}}$ towards various physical parameters.

γ_1	Sc	N_b	N_t	S_2	E_a	γ_3	$-Sh_{z_1}(Re_{z_1})^{-\frac{1}{2}}$	
							Shooting	Bvp4c
0.1							0.5472	0.5472
0.3							0.6436	0.6436
0.5							0.7365	0.7364
	0.5						0.4873	0.4873
	1.0						0.5437	0.5437
	1.5						0.6779	0.6778
		0.3					0.6277	0.6277
		0.5					0.7255	0.7255
		0.7					0.7481	0.7482
			0.3				0.5868	0.5867
			0.5				0.4259	0.4259
			0.7				0.3745	0.3744
				0.1			0.4574	0.4574
				0.3			0.5244	0.5244
				0.5			0.6376	0.6375
					0.4		0.7855	0.7854
					0.6		0.7735	0.7735
					1.2		0.7533	0.7532
						0.1	0.7873	0.7873
						0.5	0.8535	0.8535
						1.0	0.9648	0.9647
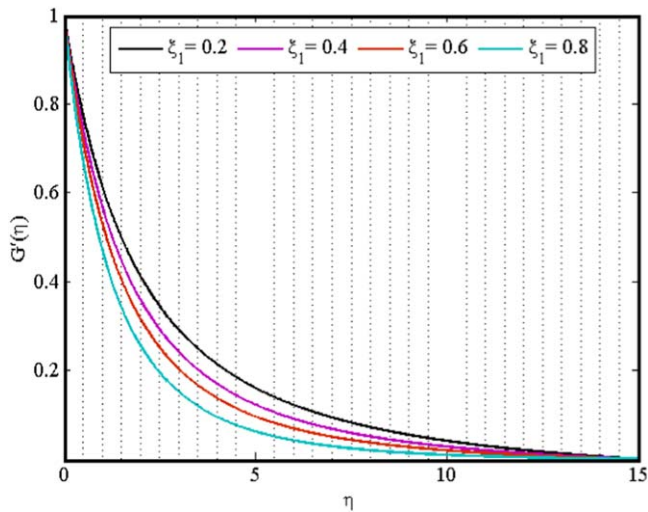
Figure 2. $G'(\eta)$ against ξ_l.
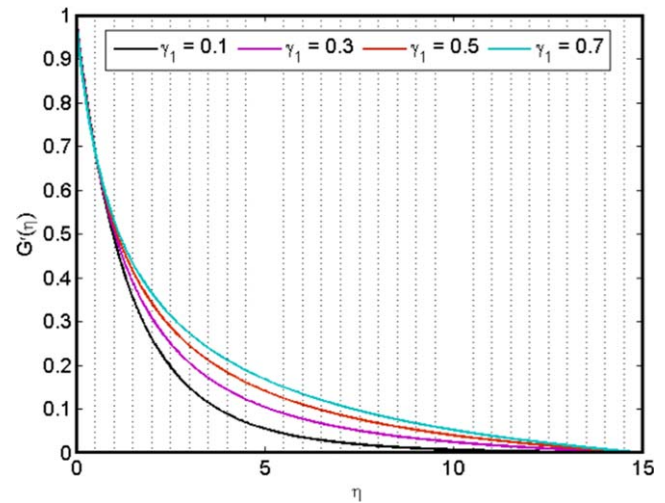
Figure 3. $G'(\eta)$ against γ_l.

The terminating benchmarks for the iterative process is set as

$$\max .\{|Z_2(15) - 0|, \ |Z_4(15) - 0|, \ |Z_6(15) - 0|\} < \varepsilon.$$

Discussion

In this section, we will explain in detail the characteristics of different physical parameters on velocity, concentration, temperature, heat and mass transfer rate in graphical and tabulated form. To analyze the results, the numerical computations are restricted thoroughly for various values of physical parameters [56] such as $(0.1 \leqslant \beta_1 \leqslant 0.5)$, $(0.2 \leqslant \gamma_1 \leqslant 0.9)$, $(0.3 \leqslant N_b \leqslant 1.4)$, $(0.4 \leqslant \xi_l \leqslant \infty)$, $(0.2 \leqslant N_t \leqslant 1.5)$, $(0.2 \leqslant \gamma_2 \leqslant 0.8)$, $(0.5 \leqslant Pr \leqslant 2.5)$, $(1 \leqslant \hat{N}_1 \leqslant 1.3)$, $(0.2 \leqslant S_v \leqslant 0.8)$, $(0.5 \leqslant N_r \leqslant 3)$, $(0.2 \leqslant M_1 \leqslant 0.5)$, $(0.2 \leqslant E_a \leqslant 1.4)$, $(0.1 \leqslant \gamma_3 \leqslant 1.0)$, $(0.2 \leqslant Sc \leqslant 1.2)$, $(0.1 \leqslant S_1 \leqslant 0.6)$ and $(0.1 \leqslant \beta_t \leqslant 0.4)$. Tables 1–3 are created to notice the significant behavior of skin friction coefficient, local Nusselt and Sherwood number towards various flow controlling parameters such as curvature parameter (γ_1), Casson fluid
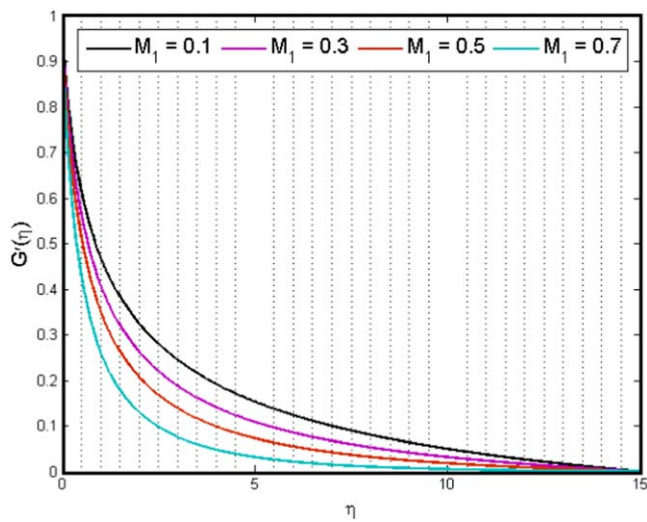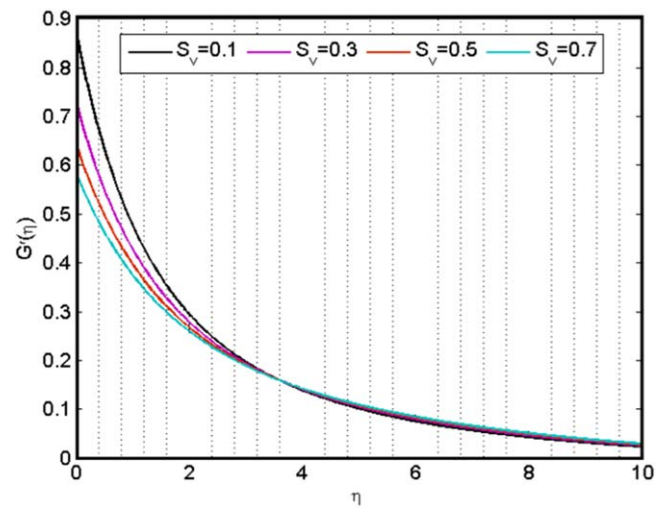
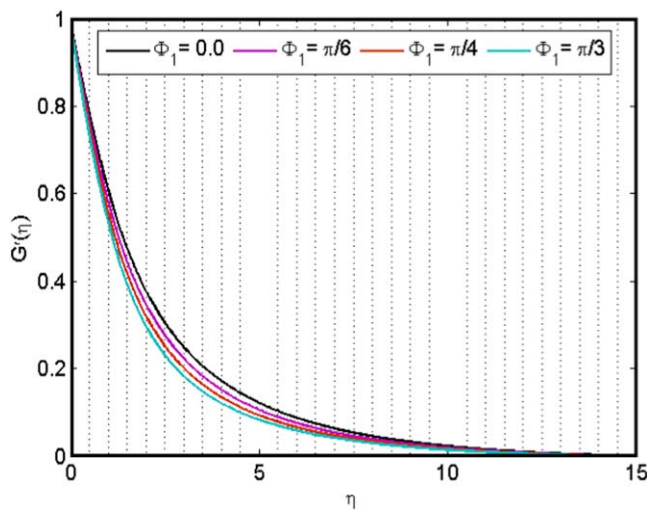**Figure 4.** $G'(\eta)$ against M_1.

Figure 7. $G'(\eta)$ against S_v.
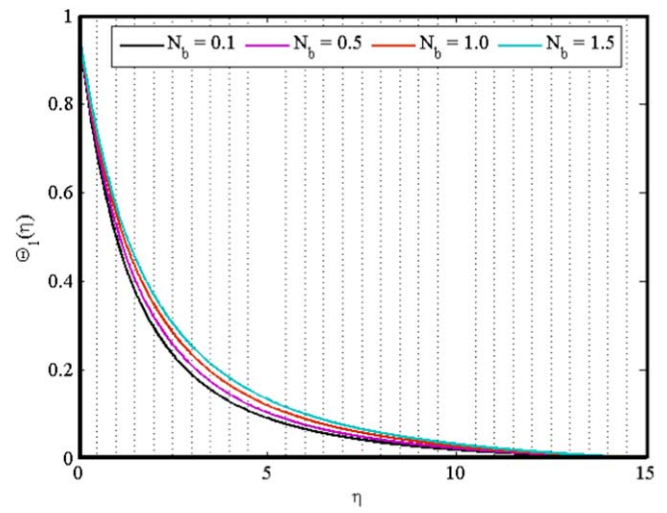

Figure 5. $G'(\eta)$ against Φ_1.

Figure 8. $\Theta_1(\eta)$ against N_b.
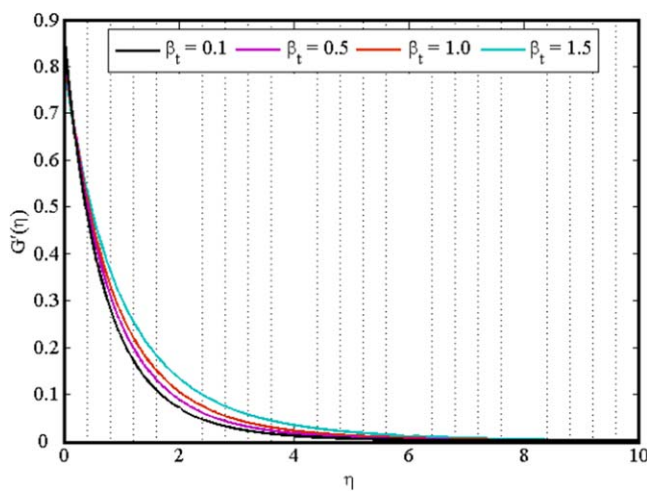

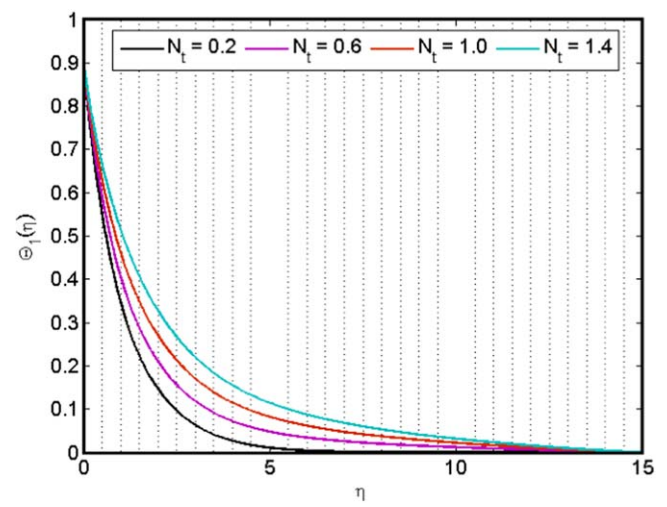**Figure 6.** $G'(\eta)$ against β_t.

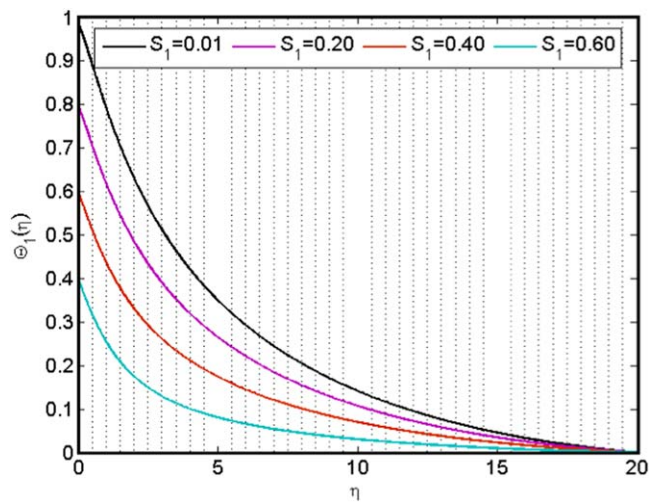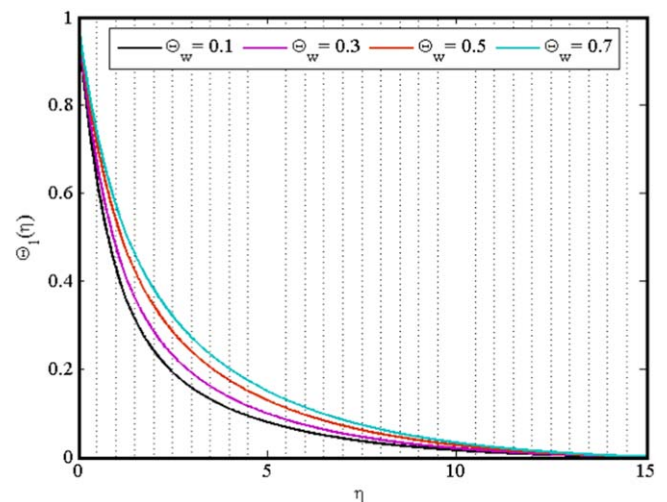**Figure 9.** $\Theta_1(\eta)$ against N_t.

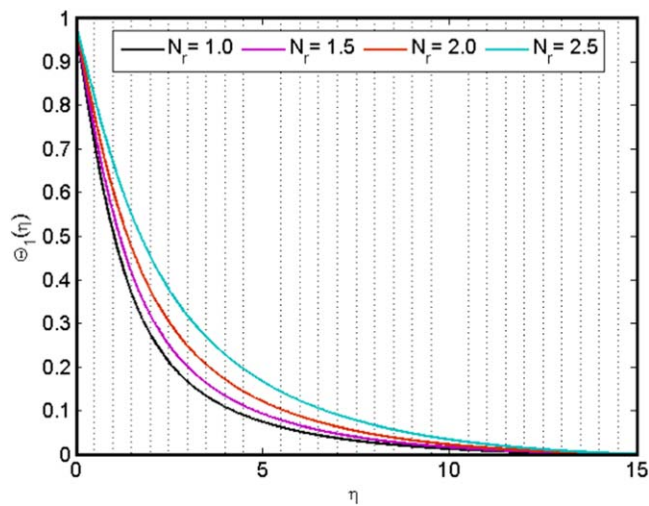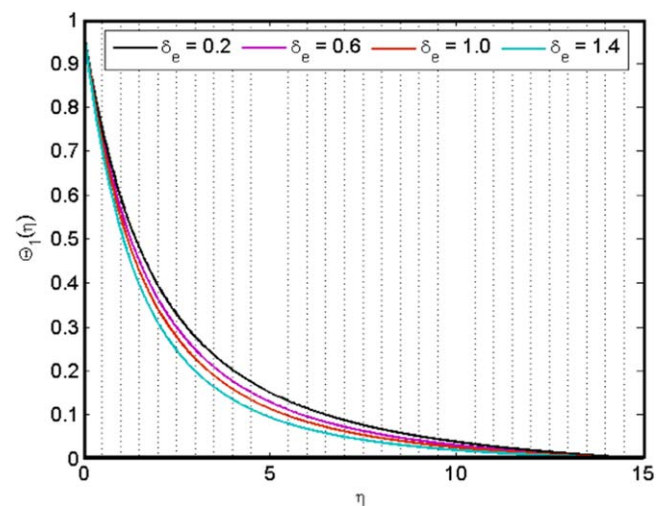**Figure 10.** $\Theta_1(\eta)$ against S_1.

Figure 11. $\Theta_1(\eta)$ against N_r.

Figure 12. $\Theta_1(\eta)$ against Pr.

Figure 13. $\Theta_1(\eta)$ against Θ_w.

Figure 14. $\Theta_1(\eta)$ against δ_e.

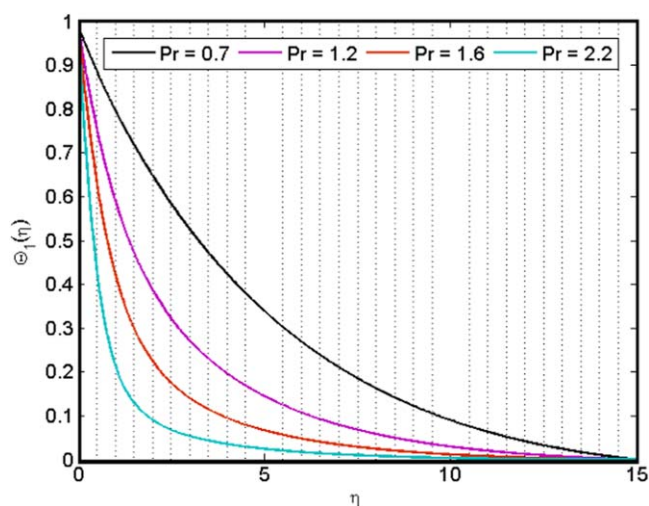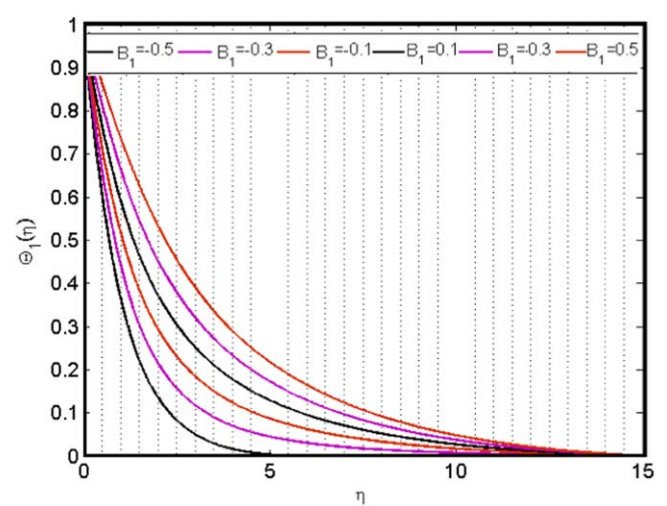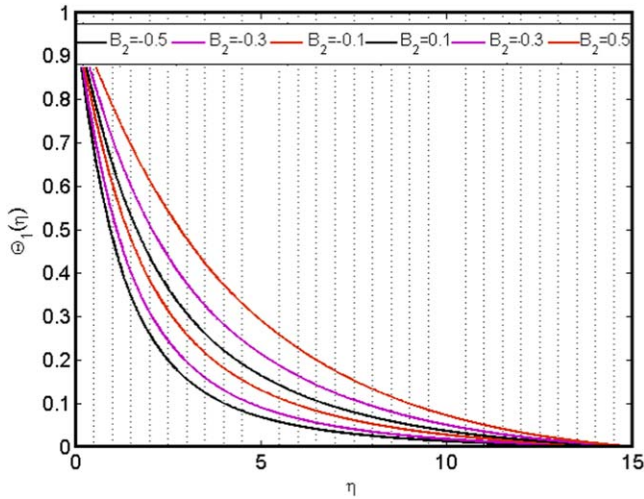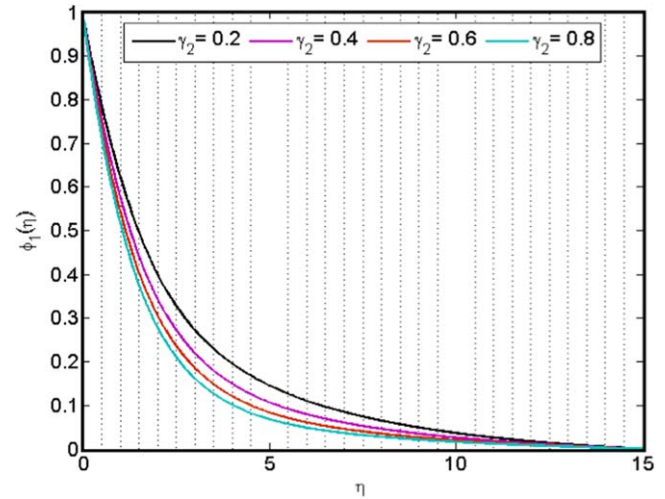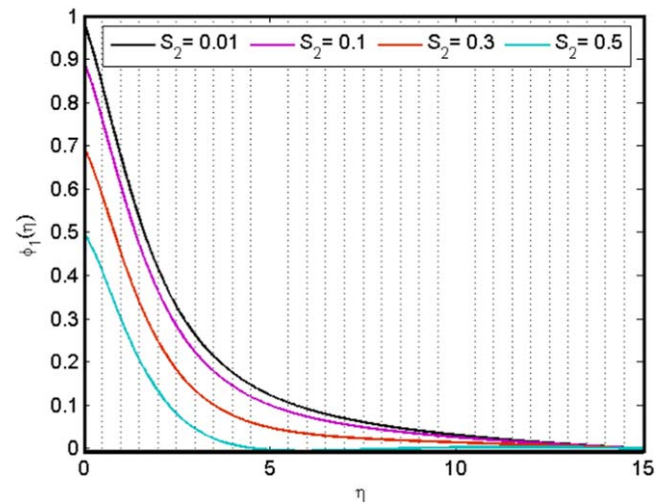**Figure 15.** $\Theta_1(\eta)$ against B_1.

Figure 16. $\Theta_1(\eta)$ against B_2.

Figure 17. $\phi_1(\eta)$ against γ_2.

Figure 18. $\phi_1(\eta)$ against S_2.

parameter (ξ_l), Hartman number (M_1), Schmidt number (Sc), mixed convection parameter (β_1), thermal radiation parameter (N_r), Brownian motion parameter (N_b), thermophorsis parameter (N_t), thermal and solutal stratification parameters (S_1, S_2), respectively. Specifically, tables 1 and 2 provide the comparison of the skin friction coefficient and local Nusselt number with the previously published results. Table 1 describes the skin friction coefficient for numerous values of (ξ_l) and (M_1) and match these values with [57] when all other parameters are kept unchanged. Without emphasis on equation (16), the present outcomes of Nusselt number for distinct values of Prandtl number are compared with existing values through table 2. We have established an excellent agreement that confirms the validity of our present work. (see tables 1 and 2). Table 3 is presented to study the sound effects of parameters like (γ_1), (ξ_l), (β_1), (M_1), (S_1), (E_a) and (S_2) on skin friction coefficient. Physically, the negative values of skin friction coefficient correspond to the amount of drag force offered by cylindrical surface to the fluid particles. It is observed that skin friction in the absolute sense, displays a provoking nature towards thermal stratification parameter (S_1), curvature parameter (γ_1), Casson fluid parameter (ξ_l) and magnetic parameter (M_1) while opposite approach is viewed for positive values of mixed convection parameter (β_1), activation energy parameter (E_a) and solutal stratification parameter (S_2) respectively. Table 4 spectacles the impact of curvature parameter (γ_1), fluid parameter (ξ_l), thermal radiation parameter (N_r), activation energy parameter (E_a), thermal relaxation parameter (δ_e), thermal stratification parameter (S_1), and (B_1) on local Nusselt number. Here, Nusselt number is an increasing function of (γ_1) and (E_a) whiles it declines for higher marks of (ξ_l), (N_r), (B_1), (δ_e) and (S_1). From table 5, it can be detected that an enhancement in curvature parameter (γ_1), Schmidt number (Sc), Brownian motion parameter (N_b) corresponds to a rise in Sherwood number, while inverse relation exists between (N_t), (E_a) and Sherwood number. The MATLAB built-in function (bvp4c) is employed for the verification of the present results obtained from the shooting code.

Velocity profiles

Figures 2–7 are portrayed to explore the features of velocity profile $(G'(\eta))$ for distinct values of (ξ_l), (γ_1), (M_1), (β_t) and (S_v). figure 2 analyze the behavior of $(G'(\eta))$ for variation of Casson parameter (ξ_l). It is observed that the velocity profile $(G'(\eta))$ declines for greater approximation of the Casson parameter (ξ_l). This is due to the fact that stress of the Casson fluid causes a decrease in rheological characteristics. When (ξ_l) approaches to its maximum value or infinity, the flow behavior resemble to the Newtonian fluid model and the fluid is able to shear faster along the surface. The effect of curvature parameter (γ_1) on velocity profile $(G'(\eta))$ is displayed in figure 3. One can see from graph that velocity distribution $(G'(\eta))$ upsurges within the frame of larger curvature parameter (γ_1). Since there exist an inverse relation between curvature and radius of cylinder. Thus, increase in (γ_1) reduces the radius of the cylinder and consequently the contact area of cylinder with fluid is abridged which produces less resistance to the fluid motion and hence enhancement of the velocity profile is noticed. Figure 4 is sketched to check the effects of
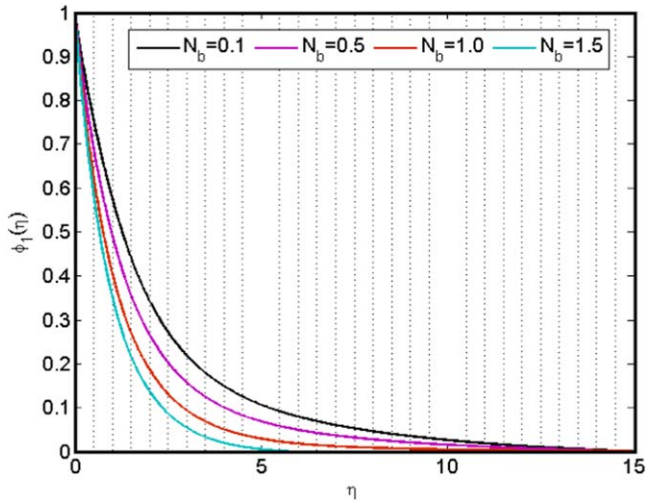
Figure 19. $\phi_1(\eta)$ against N_b.
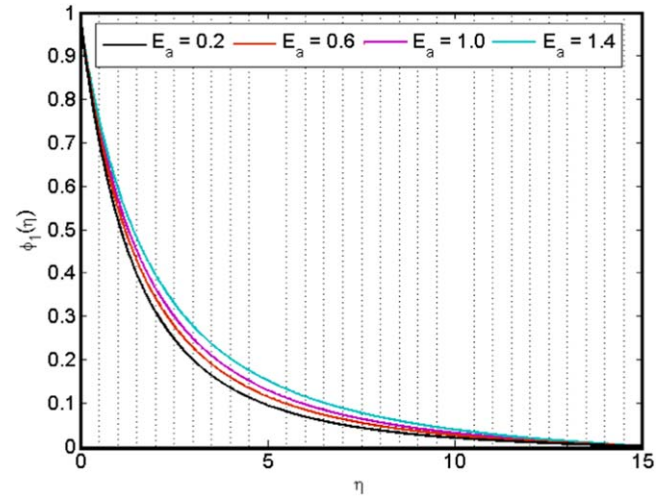
Figure 22. $\phi_1(\eta)$ against E_a.
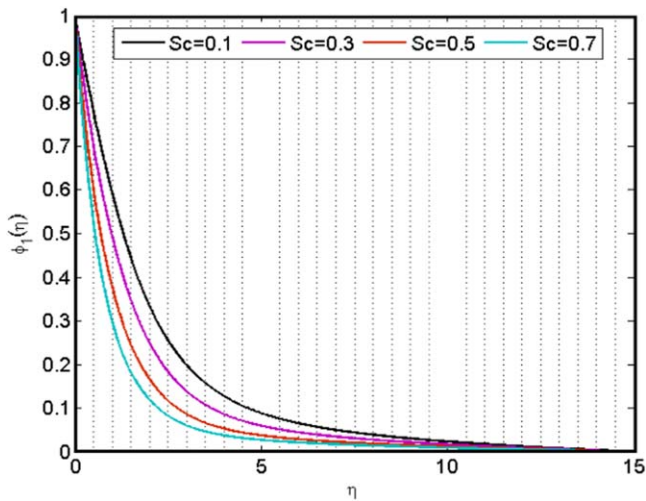
Figure 20. $\phi_1(\eta)$ against Sc.
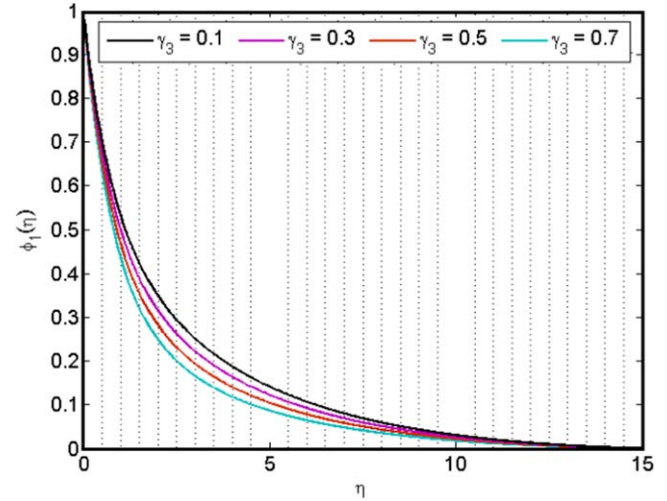
Figure 23. $\phi_1(\eta)$ against γ_3.
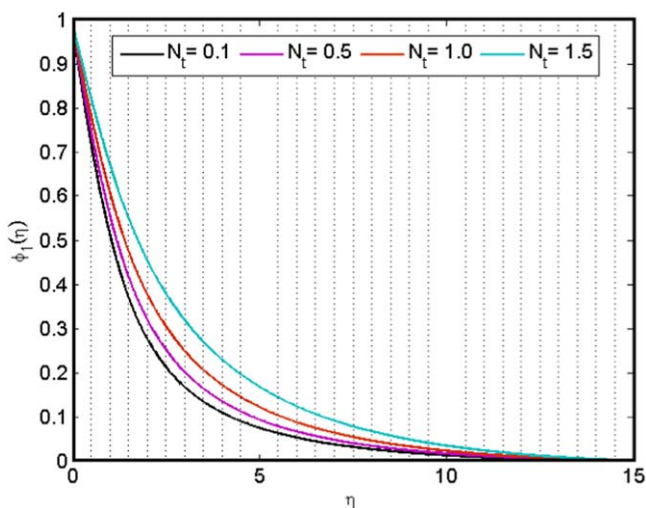
Figure 21. $\phi_1(\eta)$ against N_t.

magnetic parameter (M_1) on velocity $(G'(\eta))$. A resistive Lorentz force is developed in the flow regime, when the strength of the magnetic field is enhanced. This resistive force is responsible of decline nature in the velocity distribution. Figure 5 is revealed to analyze the effect of an inclination (ϕ_1) on velocity profile. It is observed that for greater values of (ϕ_1), the velocity profile decreases. Behavior of $(G'(\eta))$ for higher approximation of nonlinear thermal convection parameter (β_t) is presented in figure 6. Motion of fluid particles boosts up for higher marks of nonlinear thermal convection parameter (β_t). For greater approximation of (β_t), the temperature difference $(T_w - T_\infty)$ intensifies which is responsible for upsurge in velocity distribution. Impact of velocity slip parameter (S_v) on $(G'(\eta))$ is delineated through figure 7. Here the velocity $(G'(\eta))$ and momentum boundary layer thickness is lower for the growing values of velocity slip parameter (S_v). In fact, the stretching of the sheet becomes a source of

decrease in the liquid flow that weaken the velocity field $(G'(\eta))$ against velocity slip parameter (S_v).

Temperature profiles

Figures 8–16 demonstrate the behavior of Brownian motion parameter, (N_b), thermophoresis parameter (N_t), thermal radiation parameter (N_r), thermal stratification parameter (S_1), temperature ratio parameter (Θ_w), Prandtl number (Pr), thermal relaxation parameter (δ_e) and non-uniform heat source or sink parameters (B_1, B_2), respectively. Variation of Brownian motion (N_b) and thermophoresis parameter (N_t) on temperature distribution $(\Theta_1(\eta))$ is presented in figures 8 and 9. Similar enhancing behavior of both parameters (N_b, N_t) is observed for temperature $(\Theta_1(\eta))$ and apposite layer thickness. More heat is produced due to rise in random motion of the fluid particles within the frame of greater (N_b). Therefore, $(\Theta_1(\eta))$ boost ups. For larger values of thermophoresis parameter (N_t), fluid particles transport themselves from hot region to cold ones. This fact is due to boosting character of thermophoresis force that upsurges temperature profile (see figure 9). Nature of fluid temperature $(\Theta_1(\eta))$ against the variation of thermal stratification parameter (S_1) is portrayed in figure 10. It is remarked that temperature distribution $(\Theta_1(\eta))$ and associated layer thickness diminishes for greater (S_1). In fact an increase in (S_1) develops a layered configuration of fluid in vertical direction with higher density fluid at bottom than the upper region. Thus, thermal stratification (S_1) reduces the convective flow between the heated cylinder and the contiguous liquid in the medium. As a result, the temperature distribution drops. Figure 11 is designed to intricate variation in $(\Theta_1(\eta))$ for distinct standards of (N_r). Here, both temperature and its associated boundary layer thickness upsurges with an increase in thermal radiation parameter (N_r). In fact, radiation is a phenomenon that transmits energy through fluid particles. Therefore, it produces heat energy in the flow field. Due to this justification, we see the results of that type (see figure 11). Figures 12 and 13 are presented to examine the temperature distribution $(\Theta_1(\eta))$ for different estimation of Prandtl number (Pr) and temperature ratio parameter (Θ_w). One can noticed that reverse behavior exists for both parameters on temperature field. Here temperature $(\Theta_1(\eta))$ is a diminishing function of (Pr). This response of temperature $(\Theta_1(\eta))$ against (Pr) is based on weaker thermal diffusivity when compared to momentum diffusivity. Due to this argument, the temperature $(\Theta_1(\eta))$ decays. Here temperature and thermal boundary layer thickness are enhanced for greater (Θ_w). This is due to higher thermal state of liquid when compared with ambient fluid temperature. Variation of temperature $(\Theta_1(\eta))$ against non-dimensional thermal relaxation time (δ_e) is revealed in figure 14. One can grasp that temperature and apposite boundary layer thickness are weakened via larger (δ_e). In fact, material particle requires additional time for transmission of heat to its adjacent particles due to upswing in thermal relaxation parameter. Influence of space and temperature-based heat source/sink parameter $(B_1$ and $B_2)$ on temperature profile $(\Theta_1(\eta))$ is portrayed in figures 15 and 16, respectively. From these figures, it is evident that the more heat is produced for higher standards of $B_1 > 0$ and $B_2 > 0$ and this causes to enhance in $(\Theta_1(\eta))$. Although, heat is absorbed for higher values of $B_1 < 0$ and $B_2 < 0$, hence the temperature and its boundary layer dwindled.

Concentration profiles

Figures 17–23 are revealed to show the impact of (γ_2), (S_2), (N_b), (N_t), (Sc), (E_a) and (γ_3) on $(\phi_1(\eta))$. Impact of destructive chemical reaction variable $(\gamma_2 > 0)$ on concentration $(\phi_1(\eta))$ is pointed out in figure 17. Here concentration and relevant boundary layer thickness are reduced for larger destructive chemical reaction variable $(\gamma_2 > 0)$. From figure 18, it is detected that $(\phi_1(\eta))$ is a decreasing function of solutal stratification parameter (S_2). In reality, reduction in concentration potential between ambient fluid and the cylinder's surface $(C_w - C_\infty)$ is identified that ultimately lowers the concentration $(\phi_1(\eta))$ field. In figure 19 features of Brownian parameter (N_b) on $(\phi_1(\eta))$ is presented. It is observed that concentration profile is a dwindling function of (N_b). Since fluid particles are pushed in a direction opposite to the concentration gradient to make more homogeneous nanoparticle solution. Therefore, lesser concentration gradient value is noticed for greater values of (N_b). That ultimately drops the concentration $(\phi_1(\eta))$. Decreasing features of $(\phi_1(\eta))$ is found for larger approximation of Scbmit number (Sc) (see figure 20).

Due to reduction in mass diffusivity for greater (Sc), the concentration and associated boundary thickness diminishes. The increase in (N_t) contributes higher fluid thermal conductivity which spectacles the greater concentration $(\phi_1(\eta))$ as seen in figure 21. The relationship between activation energy (E_a) and nanoparticle concentration $(\phi_1(\eta))$ for particular values of parameters is analyzed in figure 22. The modified Arrhenius function dwindles with the enrichment in activation energy parameter (E_a). This finally endorses the generative chemical reaction due to which nanoparticle concentration $(\phi_1(\eta))$ upswings. Decreasing tend of $(\phi_1(\eta))$ is comprehended for larger (γ_3) (see figure 23). Physically, as we enhance…the…values…of (γ_3), the destructive rate of chemical reaction also grows which is used…to terminate/dissolve the liquid…specie…more effectively.

Conclusions

A numerical analysis is presented to investigate the influence of slip boundary conditions on a nonlinearly radiative flow of Casson nanofluid with novel impacts of activation energy, non-uniform heat generation/absorption and binary chemical reaction. Heat transfer for current problem is investigated through Cattaneo–Christove heat flux model with thermal and solutal stratification phenomena. Numerical solution of transformed system is achieved by employing shooting technique. The key observations are summarized as follows:

- Nanoparticle concentration is an enhancing function of activation energy (E_a) for chemical reaction and thermophoresis parameter (N_t). Additionally, the response of chemical reaction parameter (γ_3) is qualitatively opposite to that of (E_a).
- An enhancement in non-uniform heat generation/absorption parameters (B_1, B_2), Brownian motion and thermophoresis parameters (N_b, N_t) becomes a source of rise in temperature distribution while greater approximation of Prandlt number (Pr) and thermal relaxation parameter (δ_e) generates a plunge in temperature field.
- Temperature and concentration fields are dwindling functions of thermal and solutal stratification parameters (S_1, S_2), respectively.
- Heat transfer rate at the cylindrical surface and thermal boundary layer thickness enhances in presence of thermal radiation (N_r).
- Sherwood number has contrary behavior for larger (E_a) and (γ_3).

Acknowledgments

ORCID iDs

M Ijaz ⬤ https://orcid.org/0000-0002-2368-1959

References

[1] Magyari E and Pantokratoras A 2011 Note on the effect of thermal radiation in the linearized Rosseland approximation on the heat transfer characteristics of various boundary layer flows *Int. Commun. Heat Mass Transf.* **38** 554–6

[2] Pantokratoras A 2014 Natural convection along a vertical isothermal plate with linear and nonlinear Rosseland thermal radiation *Int. J. Therm. Sci.* **84** 151–7

[3] Cortell R 2014 Fluid flow and radiative nonlinear heat transfer over a stretching sheet *J. King Saud Univ. Sci.* **26** 161–7

[4] Parida S K, Panda S and Rout B R 2015 MHD boundary layer slip flow and radiative nonlinear heat transfer over a flat plate with variable fluid properties and thermophoresis *Alexandria Eng. J.* **54** 941–53

[5] Bhatti M, Zeeshan A and Ellahi R 2016 Study of heat transfer with nonlinear thermal radiation on sinusoidal motion of magnetic solid particles in a dusty fluid *J. Theor. Appl. Mech.* **46** 75–94

[6] Waqas M, Khan M I, Hayat T, Alsaedi A and Khan M I 2017 Nonlinear thermal radiation in flow induced by a slendering surface accounting thermophoresis and Brownian diffusion *Eur. Phys. J. Plus* **132** 280

[7] Khan M I, Tamoor M, Hayat T and Alsaedi A 2017 MHD Boundary layer thermal slip flow by nonlinearly stretching cylinder with suction/blowing and radiation *Results Phys.* **7** 1207–11

[8] Ijaz M, Ayub M and Khan H 2019 Entropy generation and activation energy mechanism in nonlinear radiative flow of Sisko nanofluid: rotating disk *Heliyon* **5** e01863

[9] Khan M I, Waqas M, Hayat T, Alsaedi A and Khan M I 2017 Significance of nonlinear radiation in mixed convection flow of magneto Walter-B nano-liquid *Int. J. Hyd. Energy* **42** 26408–16

[10] Raju C S K, Sandeep N and Saleem S 2016 Effects of induced magnetic field and homogeneous–heterogeneous reactions on stagnation flow of a Casson fluid *Eng. Sci. Tech., Int. J.* **19** 875–87

[11] Fetecau C, Jamil M and Mahmood A 2012 Flow of fractional Maxwell fluid between coaxial cylinders *Arch. Appl. Mech.* **82** 1003–1003

[12] Makinde O D, Chinyoka T and Rundora L 2011 Unsteady flow of a reactive variable viscosity non-Newtonian fluid through a porous saturated medium with a symmetric convective boundary conditions *Comput. Math. Appl.* **62** 3343–52

[13] Turkyilmazoglu M and Pop I 2013 Exact analytical solutions for the flow and heat transfer near the stagnation point on a stretching/shrinking sheet in a Jeffrey fluid *Int. J. Heat Mass Transf.* **57** 82–8

[14] Yin C, Niu J, Fu C and Tan W C 2013 Thermal convection of a viscoelastic fluid in a fluid-porous system subjected to horizontal plane Couette flow *Int. J. Heat Fluid Flow* **44** 711–8

[15] Misra J C and Pandey S K 2002 Peristaltic transport of blood in small vessels: study of a mathematical model *Comput. Math. Appl.* **43** 1183–93

[16] Mernone A V, Mazumdar J N and Lucas S K 2002 A mathematical study of peristaltic transport of a Casson fluid *Math. Comput. Model* **35** 895–912

[17] Pandey S K and Tripathi D 2010 Peristaltic transport of a Casson fluid in a finite channel: application to flows of concentrated fluids in oesophagus *Int. J. Biomath.* **3** 453–72

[18] Ijaz M and Ayub M 2019 Simulation of magnetic dipole and dual stratification in radiative flow of ferromagnetic Maxwell fluid *Heliyon* **5** e01465

[19] Bingham E C 1922 *Fluidity and Plasticity* vol 2 (New York: McGraw-Hill)

[20] Lee D Y and Wereley N M 2000 Analysis of electro and magneto-rheological flow mode dampers using Herschel–Bulkley model *Proc. SPIE* **3989** 244–52

[21] Mill C C 1959 Rheology of disperse systems (Proceedings of a conference) *Symp. Pub. Div.* (Oxford: Pergamon)

[22] Prasad P D, Saleem S, Varma S V K and Raju C S K 2019 Three dimensional slip flow of a chemically reacting casson fluid flowing over a porous slender sheet with a non-uniform heat source or sink *J. Kor. Phys. Soc.* **74** 855–64

[23] Fung Y C 1984 *Biodynamics-Circulation* (New York: Springer)

[24] Dash R K, Mehta K N and Jayaraman G 1996 Casson fluid flow in a pipe filled with a homogeneous porous medium *Int. J. Eng. Sci.* **34** 1145–56

[25] Khan M I, Waqas M, Hayat T and Alsaedi A 2017 A comparative study of Casson fluid with homogeneous-heterogeneous reactions *J. Colloid Int. Sci.* **498** 85–90

[26] Eldabe N T M and Salwa M G E 1995 Effect of magnetic field on the flow and heat transfer in a Casson thin film on an unsteady stretching surface in the presence of viscous and internal heating *J. Phys. Soc. Japan* **64** 41–64

[27] Boyd J, Buick J M and Green S 2007 Analysis of the Casson and Carreau–Yasuda non-Newtonian blood models in steady and oscillatory flows using the lattice Boltzmann method *Phys. Fluids* **19** 093103

[28] Nadeem S, Haq R U, Akbar N S and Khan Z H 2013 MHD three-dimensional Casson fluid flow past a porous linearly stretch sheet *Alex. Eng. J.* **52** 577–82

[29] Dash R K, Mehta K N and Jayaraman G 1996 Effect of yield stress on the flow of a Casson fluid in a homogeneous porous medium bounded by a circular tube *Appl. Sci. Res.* **57** 133–49

[30] Hayat T, Ijaz M, Qayyum S, Ayub M and Alsaedi A 2018 Mixed convective stagnation point flow of nanofluid with Darcy-Fochheimer relation and partial slip *Results Phys.* **9** 771–8

[31] Hayat T, Shehzad S A, Al-Sulami H H and Asghar S 2013 Influence of thermal stratification on the radiative flow of Maxwell fluid *J. Braz. Soc. Mech. Sci. Eng.* **35** 381–9

[32] Ijaz M and Ayub M 2019 Nonlinear convective stratified flow of Maxwell nanofluid with activation energy *Heliyon* **5** e01121

[33] Shehzad S A, Qasim M, Alsaedi A, Hayat T and Alhuthali M S 2013 Combined effects of thermal stratification and thermal radiation in mixed convection flow of thixotropic fluid *Eur. Phys. J. Plus* **9** 128–34

[34] Ibrahim W and Makinde O D 2013 The effect of double stratification on boundary layer flow and heat transfer of nanofluid over a vertical plate *Comput. Fluids* **86** 433–41

[35] Ijaz M, Ayub M, Zubair M and Riaz A On stratified flow of ferromagnetic nanofluid with heat generation/absorption *Phys. Scr.* **94** 045206

[36] Srinivasacharya D and Upendar M 2013 Effect of double stratification on MHD free convection in a micropolar fluid *J. Energy Math. Soc.* **21** 370–8

[37] Rehman K U, Malik M Y, Salahuddin T and Naseer M 2016 Dual stratified mixed convection flow of Eyring-Powell fluid over an inclined stretching cylinder with heat generation/ absorption effect *AIP Adv.* **6** 075112

[38] Mahmood T, Ahmed J, Shahzad A, Ali R and Iqbal Z 2016 Convective heat transfer of viscous fluid over a stretching sheet embedded in a thermally stratified medium *Bulgarian Chem. Comun.* **48** 506–13

[39] Fourier J B J 1822 *Théorie Analytique De la Chaleur* vol 6 (Paris: Didot) pp 499–508

[40] Cattaneo C 1948 Some aspects of diffusion theory *Atti Semin. Mat. Fis Univ. Modena Reggio Emilia* **3** 83–101

[41] Christov C I 2009 On frame indifferent formulation of the Maxwell-Cattaneo model of finite speed heat conduction *Mech. Res. Commun.* **36** 481–6

[42] Hadded S A M 2014 Thermal instability in Brinkman porous media with Cattaneo-Christov heat flux *Int. J. Heat Mass Transf.* **68** 659–68

[43] Sheikholeslami M, Abelman S and Ganji D D 2014 Numerical simulation of MHD nanofluid flow and heat transfer considering viscous dissipation *Int. J. Heat Mass Transf.* **79** 212–22

[44] Dhanai R, Rana P and Kumar L 2015 Multiple solutions of MHD boundary layer flow and heat transfer behavior of nanofluids induced by a power-law stretching/shrinking permeable sheet with viscous dissipation *Powder Technol.* **273** 62–70

[45] Zubair M, Ijaz M, Abbas T and Riaz A 2019 Analysis of modified Fourier law in flow of ferromagnetic Powell-Eyring fluid considering two equal magnetic dipoles *Can. J. Phys.* **97** 772–6

[46] Ayub M, Hayat T, Waqas M, Zubair M and Alsaedi A 2018 Simulation of nonlinear convective thixotropic liquid with Cattaneo–Christov heat flux *Results Phys.* **8** 1023–7

[47] Hayat T, Ayub T, Muhammad T and Alsaedi A 2017 Flow of variable thermal conductivity Oldroyd-B fluid with generalized Fourier's and Fick's laws *J. Mol. Liq.* **234** 09e17

[48] Han S, Zheng L, Li C and Zhang X 2014 Coupled flow and heat transfer in viscoelastic fluid with Cattaneo–Christov heat flux model *Appl. Math. Lett.* **38** 87–93

[49] Amanulla C H, Nagendra N and Reddy M S 2018 Computational analysis of non-Newtonian boundary layer flow of nanofluid past a semi-infinite vertical plate with partial slip *Nonlinear Eng.* **7** 29–43

[50] Ijaz M and Ayub M 2019 Activation energy and dual stratification effects for Walter-B fluid flow in view of Cattaneo–Christov double diffusion *Heliyon* **5** e01815

[51] Rehman K R, Qaiser A, Malik M Y and Ali U 2017 Numerical communication for MHD thermally stratified dual convection flow of Casson fluid yields by stretching cylinder *Chin. J. Phys.* **55** 1605–14

[52] Raju C S K, Hoque M M and Sivasankar T 2017 Radiative flow of Casson fluid over a moving wedge filled with gyrotactic microorganisms *Adv. Powder Tech.* **28** 575–83

[53] Ijaz M, Ayub M, Y M, Khan H and Aly S 2019 Entropy analysis in nonlinearly convective flow of Sisko model in presence of Joule heating and activation energy: Buongiorno model *Phys. Scr.* (accepted) (https://doi.org/10.1088/ 1402-4896/ab2dc7)

[54] Khan M I, Waqas M, Hayat T, Khan M I and Alsaedi A 2017 Numerical simulation of nonlinear thermal radiation and homogeneous-heterogeneous reactions in convective flow by a variable thicked surface *J. Mol. Liqs.* **246** 259–67

[55] Amanulla C H, Wakif A, Boulahia Z, Suryanarayana Reddy M and Nagendra N 2018 Numerical investigations on magnetic field modeling for Carreau non-Newtonian fluid flow past an isothermal sphere *J. Braz. Soc. Mech. Sci. Eng.* **40** 462–77

[56] Turkyilmazoglu M 2016 Determination of the correct range of physical parameters in the approximate analytical solutions of nonlinear equations using the adomian decomposition method *Mediterranean J. Math.* **13** 4019–37

[57] Nadeem S, Haq R U and Lee C 2012 MHD flow of a Casson fluid over an exponentially shrinking sheet *Sci. Iranic.* **19** 1550–3

[58] Mukhopadhyay S 2013 MHD boundary layer flow and heat transfer over an exponentially stretching sheet embedded in a thermally stratified medium *Alexandria Eng. J.* **52** 259–65

[59] Bidin B and Nazar R 2009 Numerical solution of the boundary layer flow over an exponentially stretching sheet with thermal radiation *Eur. J. Sci. Res.* **33** 710–7